Journal of Asian Earth Sciences 237 (2022) 105360

Contents lists available at ScienceDirect

Journal of Asian Earth Sciences

journal homepage: www.elsevier.com/locate/jseaes

The boundary between the North China Craton and the Central Asian Orogenic Belt in NE China: Seismic evidence from receiver function imaging

Weiyu Dong [a,c], Tao Xu [a,d,*], Yinshuang Ai [b,c,d,*], Enbo Fan [b,c], Long Li [b,c], Jue Hou [a,c,e]

[a] State Key Laboratory of Lithospheric Evolution, Institute of Geology and Geophysics, Chinese Academy of Sciences, Beijing 100029, China
[b] Key Laboratory of Earth and Planetary Physics, Institute of Geology and Geophysics, Chinese Academy of Sciences, Beijing 100029, China
[c] University of Chinese Academy of Sciences, Beijing 100049, China
[d] Innovation Academy for Earth Science, CAS, Beijing 100029, China
[e] Institute of Geophysics, China Earthquake Administration, Beijing 100081, China

ARTICLE INFO

Keywords:
North China Craton
Central Asian Orogenic Belt
NE China
Receiver function imaging

ABSTRACT

This study imaged the crustal structure and tectonic state of the interacting North China Craton (NCC) and Central Asian Orogenic Belt (CAOB) using receiver function imaging. The seismic profile derived from the NCISP-10 broadband seismic array spanning a northeasterly area of the NCC and a southeasterly area of the CAOB. The profile shows a flat Moho with localized anomalies but generally resting at an average depth of 32 km. The average Vp/Vs ratio was about 1.75 but the crust around the Songliao Basin exhibits a relatively high Vp/Vs ratio and a shallow Moho. An obvious velocity discontinuity appears within the crust beneath the Songliao Basin as evidenced by theoretical model tests which managed effects from multiple waves generated by sedimentary layers in the basin. This discontinuity inclines gently and is interpreted to represent the deep extension of the Chifeng-Kaiyuan fault (CKF), which itself serves as the surface boundary between the NCC and CAOB. The NCC feature appears to the south of this boundary, while a nappe structure formed during subduction-collision and composed primarily of a subduction-accretionary complex lies to the north. The Tanlu Fault consists of two branches in the study area, the Yilan-Yitong fault (YYF) and the Dunhua-Mishan fault (DMF). The YYF cuts through the Moho and has a vertical offset of 2–3 km indicating that it represents a crustal-scale normal fault. The DMF gives no obvious indication of vertical offset in the images but may be mainly characterized by sinistral strike slip movement.

1. Introduction

Cratons and orogenic belts are first-order tectonic units that make up the Earth's lithosphere. As 'welds' between cratons, orogenic belts join different blocks into a broader continent. The North China Craton (NCC) is one of the oldest cratons in the world (Santosh et al., 2009; Tang et al., 2016). The Central Asian Orogenic Belts (CAOB) to its north represents one of the largest paleo-accretionary orogenic belts in the world and an area exhibiting some of the most significant crustal growth observed among Phanerozoic bodies (Kröner et al., 2014; Liu et al., 2017; Wilde, 2015). The CAOB formed due to two-way, asymmetric accretion wherein southward accretion establishes a subduction-accretionary complex that covers a much wider area than that formed by northward accretion. The Solonker-Xilamuren-Changchun-Yanji suture joins the two accreted margins (Liu et al., 2017; Wu et al., 2007; Xiao et al., 2003).

Studies have shown that northern margin of the NCC resembles an Andean-type continental margin which experienced long-term or multi-stage modification by southward subduction of the Paleo-Asian Ocean plate beneath the NCC (Xiao et al., 2003; Xiao et al., 2015; Zhang et al., 2007; Zhang et al., 2009). Consequently, better understanding of structural interactions between the NCC and CAOB can help resolve the evolution of the CAOB and inform models of continental formation and growth. The deep boundary between the NCC and CAOB remains an area of significant uncertainty. While general consensus holds that the Chifeng-Kaiyuan fault (CKF) represents the surface boundary between

* Corresponding authors at: State Key Laboratory of Lithospheric Evolution, Institute of Geology and Geophysics, Chinese Academy of Sciences, Beijing 100029, China (T. Xu). Key Laboratory of Earth and Planetary Physics, Institute of Geology and Geophysics, Chinese Academy of Sciences, Beijing 100029, China (Y. Ai).
E-mail addresses: xutao@mail.iggcas.ac.cn (T. Xu), ysai@mail.iggcas.ac.cn (Y. Ai).

https://doi.org/10.1016/j.jseaes.2022.105360
Received 9 December 2021; Received in revised form 28 July 2022; Accepted 30 July 2022
Available online 4 August 2022

the NCC and CAOB (Fig. 1; Xiao et al., 2003; Zhang et al., 2014), very little evidence exists for this interpretation due to Cenozoic sedimentary cover obscuring the fault. Other characteristics of the boundary at depth remain unclear as well, and few geophysical studies have addressed these areas of uncertainty.

This study used broadband seismic data from Kuandian County, Dandong City, Liaoning Province to Tongliao City, Inner Mongolia (NCISP-10 in Fig. 1) to perform receiver function imaging of crustal structure. Results elucidate the deep boundary between the NCC and the CAOB.

2. Geological background

The NCC is the oldest craton in China. It is wedge-shaped and bound by three Phanerozoic orogenic belts. The CAOB (the eastern section) lies to the north, the Qinling-Dabie-Sulu orogenic belt lies to the south, and the western Pacific subduction zone lies to the east (Meng and Zhang, 2000; Wu et al., 2020, 2021). Structural and other aspects of the orogenic belts indicate that eastern sections of the CAOB and Qinling-Dabie-Sulu belt were conjoined with the eastern part of the NCC but were then transformed by subduction of the western Pacific to become an active continental margin.

The study area addressed herein spans the northeastern part of the NCC and the southeastern edge of the CAOB. The basement of the NCC in the study area consists of Archean to Paleoproterozoic metamorphic rocks, overlying Mesoproterozoic to Early Paleozoic (Cambrian-Ordovician) marine sedimentary strata, Carboniferous-Permian alternating marine-continental sedimentary units, and Mesozoic volcanic-sedimentary strata deposited in fault basins (Santosh et al., 2009; Tang et al., 2016; Yang et al., 2016; Zhai and Santosh, 2013; Zhao et al., 2005; Zhao and Zhai, 2013).

The CAOB (eastern section) formed from the closure of the Paleo-Asian Ocean between the NCC and the Siberian Craton. Present consensus holds that the Xar Moron River suture zone located along the north side of the NCC represents the final suture zone of the Paleo-Asian Ocean. During the Paleozoic, the Paleo-Asian Ocean plate subducted beneath the NCC to form an Andean-type continental margin along the northern edge of the NCC (He et al., 2021; Windley et al., 2007; Xiao et al., 2003, 2015; Zhang et al., 2014). In the Early to Middle Triassic, collision of the southern accreted margin of Siberia (southern Mongolia) and the Andean-type northern margin of the NCC formed large-scale nappe structures representing thrusting of subduction-accretionary materials over the NCC (Zhang et al., 2014).

Since the Early Cretaceous, the Pacific plate has subducted downwards beneath the Asian continent to form extensive intermediate acid magmatism and related large-scale igneous rocks throughout the eastern NCC and CAOB. A series of extensional basins and metamorphic core complexes also formed during this interval. Westward subduction of the Pacific plate is considered to be the main controlling factor for Mesozoic lithospheric thinning and destruction of the craton around north and northeast China (Chen et al., 2008; Lei and Zhao, 2005, 2006; Wu et al., 2005; Zhang et al., 2012, 2014, Zhu et al., 2012, 2015; Meng et al., 2021). The NCC and eastern sections of the CAOB thus bear evidence of Mesozoic magmatism, metamorphic core complex formation, and other major crust forming events, but the images at depth remain uncertain.

3. Data and method

The seismic observation data used in this paper came from 38 broadband seismic stations deployed by the Key Laboratory of Earth and Planetary Physics, Chinese Academy of Sciences in Liaoning Province. The profile extends from southeast to northwest, starting from Kuandian County, Dandong City, Liaoning Province and ending at Tongliao City, Inner Mongolia. The inter-station spacing in Liaoning Province is about 10 km, and that in Inner Mongolia is about 15 km. This gave sufficient, high quality data for a profile reaching a total length of nearly 400 km (Fig. 1). Data collection spanned about 21 months from October 2016 to July 2018.

Receiver functions represent time series containing the wave propagation response of the medium beneath the station. The response is

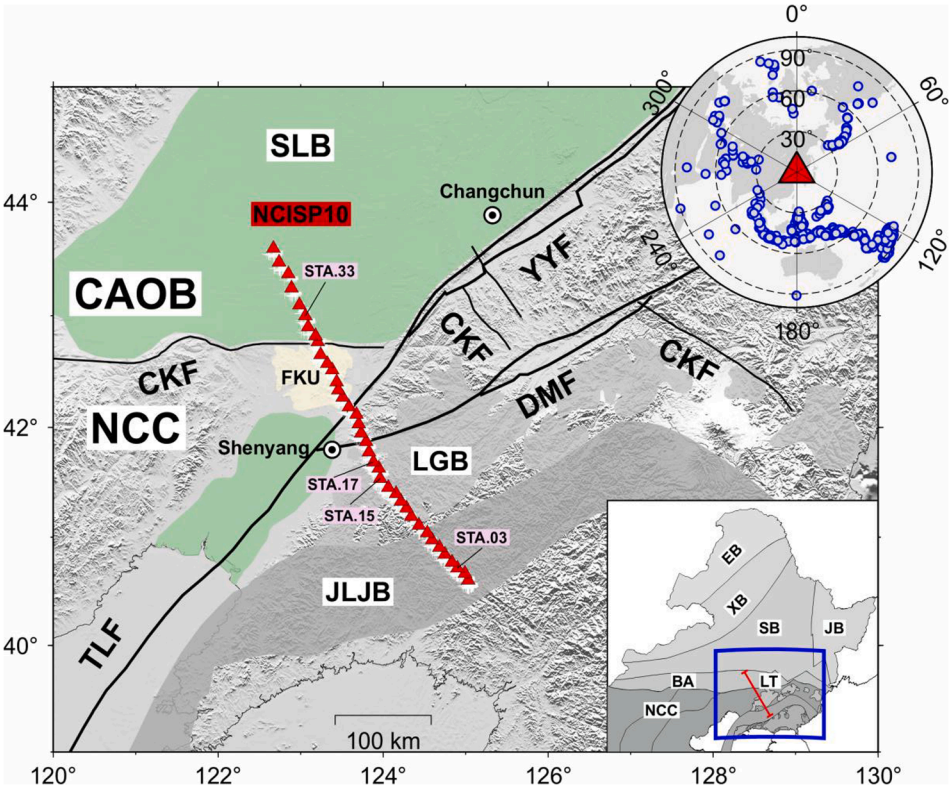

Fig. 1. Location, geological structure, and station distribution for the study area. The red triangles represent stations. The blue circles in upper inset represent effective seismic events at 30 – 90° epicentral distance from the study area. SLB: Songliao basin; FKU: Faku uplift; TLF: Tanlu Fault; CKF: Chifeng-Kaiyuan fault; YYF: Yilan-Yitong fault; DMF: Dunhua-Mishan fault; EB: Erguna block ; XB: Xing'an block; SB: Songliao block; JB: Jiamusi block; LT: Liaoyuan terrane ; NCC: North China Craton; CAOB: Central Asian Orogenic Belt; BA: Bainaimiao Arc. (For interpretation of the references to colour in this figure legend, the reader is referred to the web version of this article.)

detected by deconvolving the vertical component from the radial (or tangential) component recorded by the near-vertical incident teleseismic signal in the time domain. This paper used teleseismic events at epicentral distances of 30°-90° from the study area. The event records were subjected to 0.01–5 Hz band-pass filtering and then used to calculate the radial receiver function of teleseismic P waves. Deconvolution used an iterative time-domain deconvolution proposed by Ligorría and Ammon in 1999 (Ligorrfa and Ammon, 1999). A Gaussian filter with a coefficient of 5.0 was used to filter receiver functions. A total of 2399 receiver functions of sufficient quality were selected to optimize the signal-to-noise ratio of the stacking signal (Fig. 2 as an example).

The H-κ stacking technique was used to determine crustal thickness (H) and Vp/Vs ratio (κ) in the subsurface beneath a given station (Zhu, 2000a, 2000b). This research used an H search range of 20–60 km and step size of 0.1. The κ search range of 1.5–2.0 used a step size of 0.01. The weights of three seismic phases (Pms, Ppps, Ppss&Psps) were 0.5, 0.3, and 0.2 respectively. Better signals received higher weights (Fig. 3).

We also carried out common conversion point (CCP) stacking of images. This method varies grid size and background velocity model to optimize resolution, image intensity and image accuracy. The horizontal grid size was set to 5 km, and the vertical grid size was set to 1 km. The background velocity model refers to the ambient noise results of the same profile and derives separately for each station. For stations above major sedimentary cover, we used the H-β method (Tao et al., 2014) and the Horizontal-to-Vertical Spectral Ratio (HVSR) method (Bao et al., 2018) to determine the thickness and velocity of the sedimentary layer. The H-β method can obtain the velocity and thickness of the layers by minimizing the S wave energy flux from the half space to the layers, since the upgoing S wavefield is absent in the half-space. The HVSR method extracts the frequency responses of the seismic impedance between the sediment and the basement, further inverts for the S wave velocity. The two methods helped resolve the background velocity model.

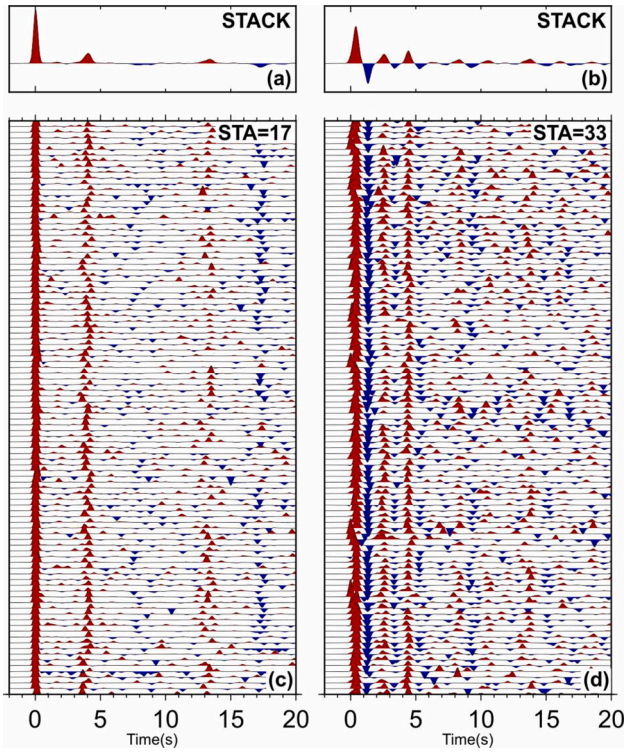

Fig. 2. (a) and (b) show stacking receiver functions of stations 17 and 33; (c) and (d) are the effective receiver functions calculated for the two stations, respectively. Station 33 is located within the Songliao Basin, affected by sedimentary layer, while station 17 is not.

The northeast part of the study area represents southerly areas of the Songliao Basin which host thick Mesozoic cover at the surface. Receiver functions calculated following the above methods included multiple waves from sedimentary cover that mask phases representing deeper crustal structure. To discern real phases from multiples, we modeled major signals and multiples under interference generated by sedimentary cover. Different velocity models were also used to calculate the theoretical receiver function. The real velocity structure was determined by comparing theoretical results with observations. We also used a resonance removal filter to remove the influence of multiples (Yu et al., 2015). The basic steps of this process were as follows. First, the receiver function affected by sedimentary cover was subjected to autocorrelation to determine the strength and two-way travel time for multiples. The two parameters were then used to define a specific filter in the frequency domain. The receiver function was then filtered to eliminate the influence of the multiple.

4. Receiver function imaging results

4.1. Characteristics of crustal structure

Calculation of receiver function (Figs. 2 and 4), CCP imaging (Fig. 5) and H-κ stacking (Fig. 6) revealed the Moho depth and lateral variation, average crustal Vp/Vs ratio, and the major intracrustal discontinuities within the study area.

The Moho specifically rests at an average depth of about 32 km, where it forms a relatively flat feature with a maximum depth difference of about 4–5 km. Beneath the JLJB in the southeast, the Moho appears at greater depths of about 34 km. In the Tanlu Fault Zone between the YYF and the DMF, the Moho appears shallower with its shallowest depth being less than 30 km. Recent studies have also shown this feature of Moho (Zhang et al., 2020; Yang et al., 2019). Beneath the Songliao Basin, Moho phase arrival time in receiver functions indicates a deeper Moho. This result is influenced by the velocity model selection in the time-depth conversion process and low velocities associated with the sedimentary layer beneath the basin, so that clarification would require more accurate sedimentary P- and S-wave velocities as inputs to CCP stacking steps. We used the H-β method (Tao et al., 2014) and the horizontal-to-vertical spectral ratio method (Bao et al., 2018) to constrain the thickness and velocity of the sedimentary layer. We then applied this in time-depth conversion steps to obtain a relatively accurate Moho depth estimate of about 30–33 km beneath the Songliao Basin (Fig. 5).

The 38 stations of the array gave an average Vp/Vs ratio of about 1.75, which showed little change throughout the study area. In the southeast of the study area, the JLJB's wave velocity ratio showed only minor lateral variation. The junction of the LGB showed more obvious change, which may relate to the formation of the orogenic belt and magmatic activity. The Tanlu Fault Zone between the YYF and the DMF exhibited a low Vp/Vs ratio anomaly. This may reflect magmatic activity controlled by major faults in the region. To the northwest, a higher Vp/Vs ratio appears beneath the Songliao Basin. The transition from low to high Vp/Vs ratio occurs in a southeast to northwest direction. A gradual feature like this may reflect the gradual decrease of cratonic components along the contact zone between the NCC and CAOB (Fig. 6a). The use of the H-β method in querying low-velocity characteristics of the sedimentary layer lend credibility to the Vp/Vs ratio and Moho depth estimates.

The Tanlu Fault is one of the largest faults in the eastern part of Eurasia, and its branch, the YYF, affects the Moho interface. This suggests that Tanlu Fault is a deep feature that cuts through the Moho, or a crustal-scale fault. The DMF shows no obvious evidence of cutting and displacing the Moho in the profile (Fig. 5).

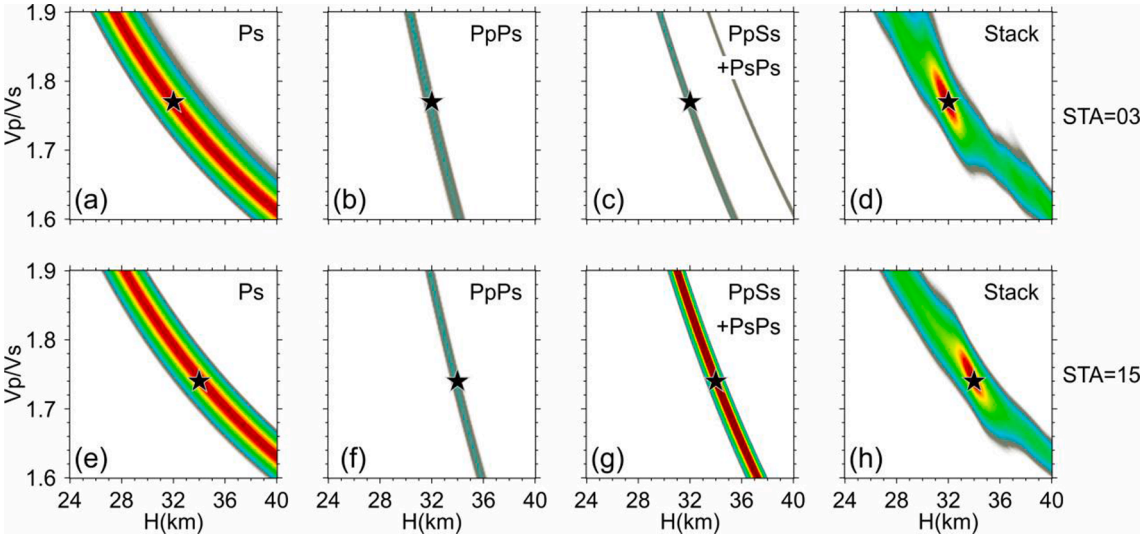

Fig. 3. Results of the H-κ grid search for stations 03 and 15. (a) - (c) and (e) - (g) represent the searching results for the three seismic phases (Ps, PpPs and PsPs + PpSs). (d) and (h) show the stacking results of the three phases respectively. Black stars represent the optimal solution.

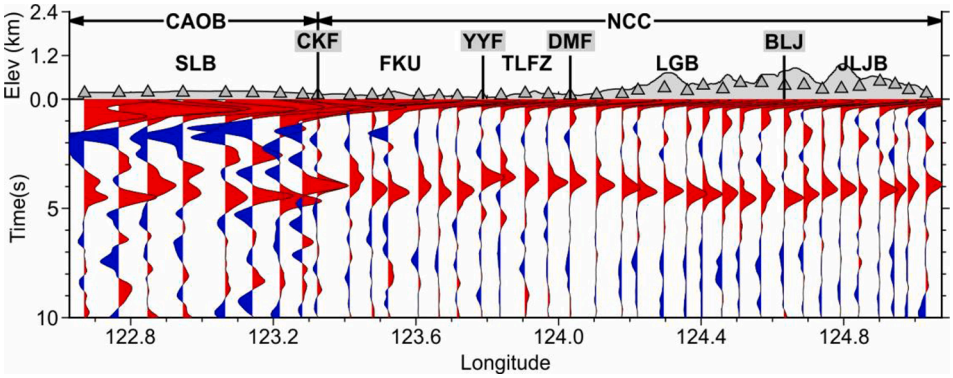

Fig. 4. Single station stacking results of receiver function. BLJ refers to the Boundary between LGB and JLJB. TLFZ refers to the Tanlu Fault Zone, and other abbreviations are similar to those in Fig. 1.

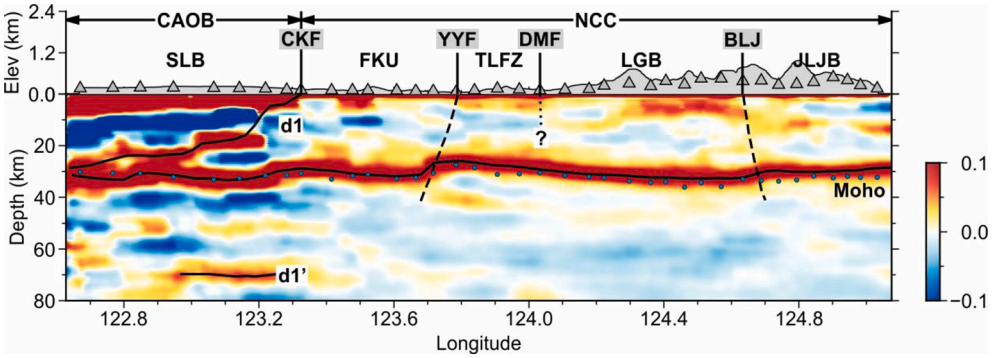

Fig. 5. CCP stacking result of all 2399 receiver functions and profile elevation above. The solid black line represents the main velocity discontinuity including Moho and discontinuity in the crust. The black dotted line represents the extension of the main faults in the subsurface. The blue dots represented the Moho depth from H-κ stacking. d1 and d1′: Target seismic phase and its multiple phase. Other abbreviations are similar to those in Fig. 1 and Fig. 4. (For interpretation of the references to colour in this figure legend, the reader is referred to the web version of this article.)

4.2. Character of discontinuities in the crust

The Songliao Basin crust exhibits a strong positive seismic phase. The CCP images show this feature within the middle and lower crust (Fig. 5-d1). Stacked receiver functions of each single station indicate it likely extends from the surface to the Moho (Fig. 4). The lack of continuity in the upper crust may due to the concealment of the negative seismic phase from the sedimentary cover and limitations in receiver function imaging of steep-angle interfaces. A thick sedimentary layer can reflect seismic waves multiples such that the receiver function will record strongly alternating, high amplitude phases that conceal and interfere with other phases. Detection of seismic phases beneath the sedimentary layer requires steps to manage the influence of multiples. Because the Songliao Basin hosts a massive accumulation of sediment, detection focusses on the strong positive seismic phase in the crust below, which we call target phase. Its possible corresponding velocity discontinuity is referred to as the target interface.

The CCP results show a relatively strong positive seismic phase at 70

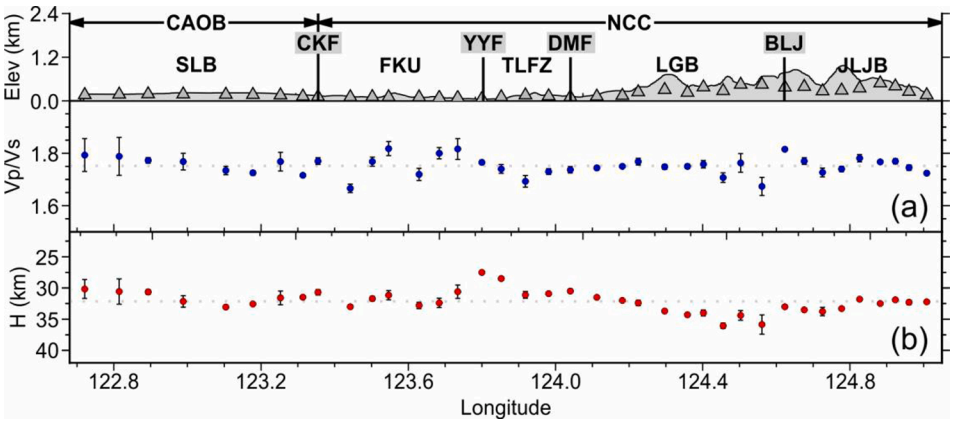

Fig. 6. Moho depth and crustal Vp/Vs ratios for each station after H-κ stacking. (a) Vp/Vs ratio represented by the blue dots; (b) Moho depth represented by the red dots. The shorter black bar represents the error calculated by the Bootstrap algorithm. Abbreviations for faults and terranes are similar to those in Fig. 1 and Fig. 4. (For interpretation of the references to colour in this figure legend, the reader is referred to the web version of this article.)

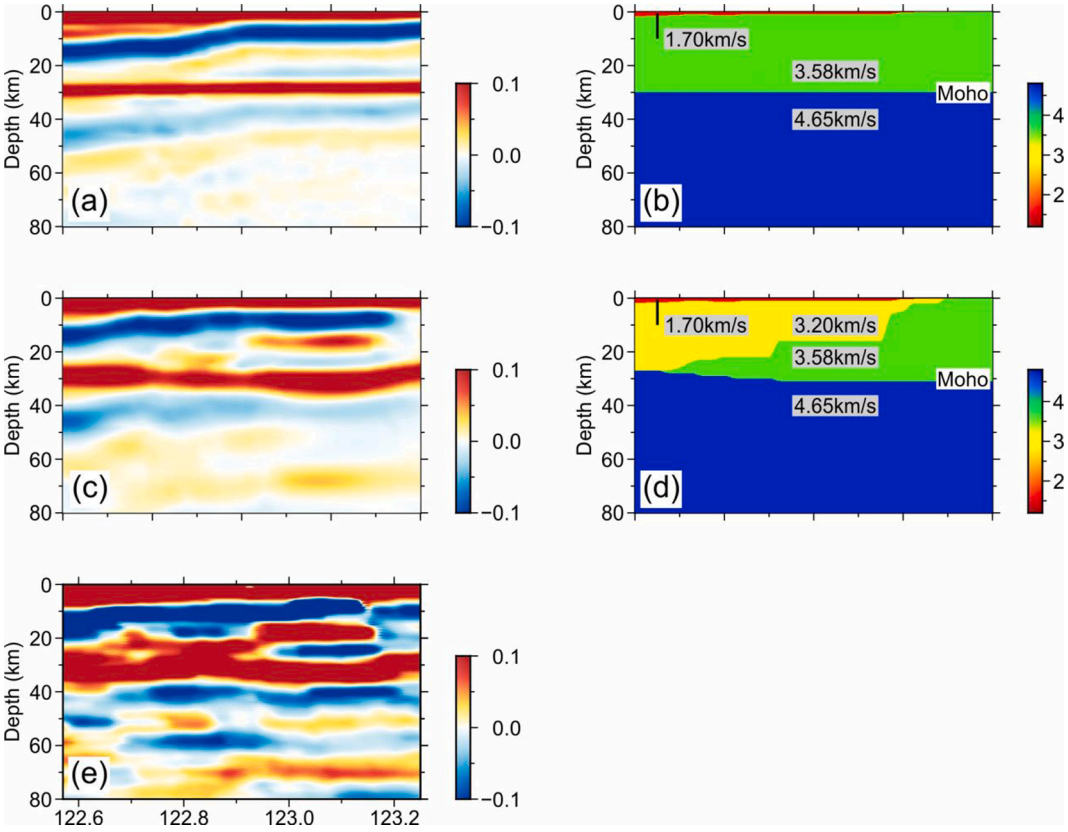

Fig. 7. Two-dimensional forward modeling of receiver functions covering the Songliao Basin (Velocity model and CCP result). (a, b) Model 1 (sedimentary layer + Moho) velocity structure and its forward receiver function CCP result; (c, d) Model 2 (sedimentary layer + target layer + Moho) velocity structure and its forward receiver function CCP result; (e) Observational data receiver function CCP result.

km depth beneath the Songliao Basin (Fig. 5-d1). Theoretical deduction and forward calculation indicate that the multiple waves of the sedimentary layer attenuate rapidly as depth increases. This feature would be inconsistent with a strong seismic phase at 70 km and warrant further consideration of possible intracrustal interfaces. We designed a target interface within the crust for a target seismic phase, obtained the receiver function through forward calculation, and adjusted the velocity model to obtain the best fit between the theoretical and observational results (Fig. 7a-d). The model with the target interface provided much better results than the model without the target interface. The former fits the arrival time and amplitude of the target phase and its multiples. Fitting of the amplitude did not take the form of an absolute numerical value but rather a relatively large amplitude value proposed for the gradually attenuated feature. Comparison of the models indicates that the target phase corresponds to a real velocity discontinuity in the crust. The target interface (Ps) and its multiple seismic phases (PpPs) appear in the stacking receiver function of a single station (Fig. 8b and d). Specific H-κ stacking was performed to obtain the average depth and average Vp/Vs ratio for the target interface, taking station 33 and 35 as an example (Fig. 8a and c). Consistency with the hypothetical model containing the target interface demonstrates the validity of the target interface.

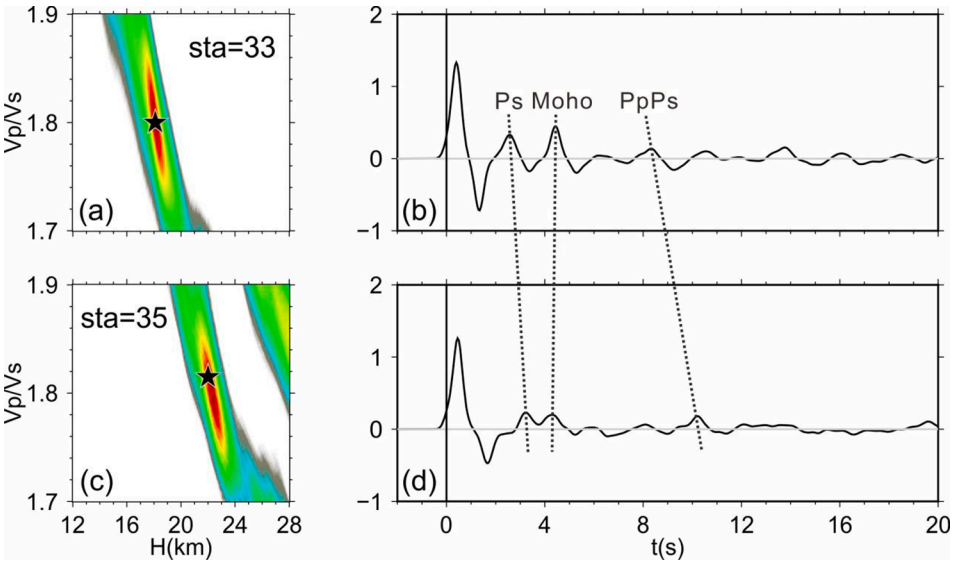

Fig. 8. H-κ stacking examples (a, c) and corresponding stacking receiving function (b, d) of the stations in the Songliao Basin against the target discontinuity. The black stars represent the optimal solution of H and κ obtained by the H-κ stacking. The three dotted lines in (b, d) represent the target phase (Ps) and its multiples (PpPs), Moho phase.

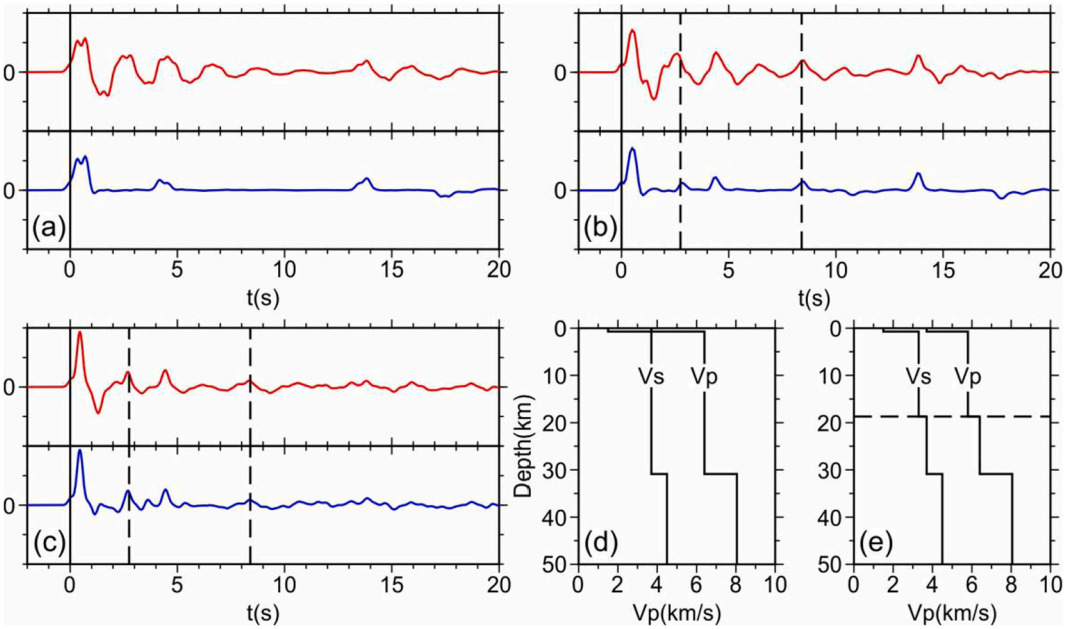

Fig. 9. Theoretical model test and application of observation data to remove multiples from sedimentary layers (station 33 as an example). (a) Model 1 (sedimentary layer + Moho) to remove the multiple wave test of the sedimentary layer; (b) Model 2 (sedimentary xlayer + target layer + Moho) to remove the multiple wave test of the sedimentary layer; (c) Observation data to remove sedimentary layer multiple wave test (station 33); (d) Velocity model 1; (e) Velocity model 2. The red solid line represents the receiving function before processing; the blue solid line represents the received function after processing; the dashed line represents the target discontinuity or its multiples. (For interpretation of the references to colour in this figure legend, the reader is referred to the web version of this article.)

Additional verification used a resonance removal filter to remove or reduce reverberations associated with a low-velocity sedimentary layer (Yu et al., 2015). This method assumes a nearly horizontal velocity discontinuity and a simple velocity structure. Station 33 offered a small vertical change of the target seismic phase suitable for verification. Before applying these steps to observational data, we first tested the theoretical receiver function and also designed two velocity models (with and without target interfaces, Fig. 9d and e) to calculate the theoretical receiver function. The velocity models were optimized to fit the station 33 receiver function observations. After processing the resonance removal filter, the model returns a receiver function calculated without the target interface. Multiples of the sedimentary layer are suppressed (Fig. 9a and b). Processing of the corresponding receiver function containing the target interface suppresses the sedimentary seismic phase retaining the target seismic phase (Dotted line in Fig. 9b). The above processing demonstrates the reliability of the method and can be further applied to observational data. Observational data results retained the target seismic phase after processing (Fig. 9c). This result is more consistent with the model containing the target interface and validates the interpretation that the target corresponds to a real velocity discontinuity in the crust.

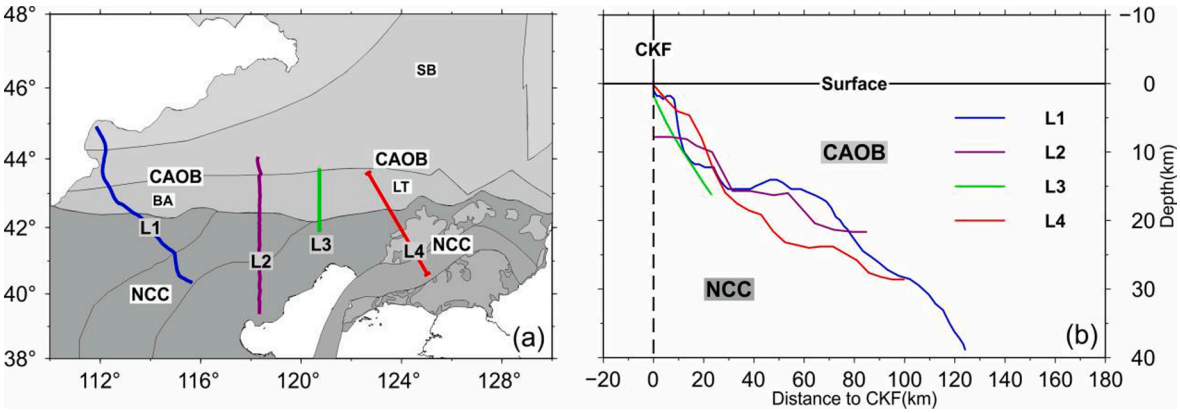

Fig. 10. Comparison of relevant, analogous profiles from surrounding regions. (a) Location of profile; (b) Comparison of the deep extension of the structural boundary between the NCC and the accretionary block from different profiles. The horizontal axis represents vertical distance from the boundary line to the CKF, and the vertical axis represents depth. L1-Deep reflection profile ; L2-Receiver function profile ; L3-Magnetic sounding profile ; L4-Receiver function profile in this paper.

5. Discussion

5.1. Deep structure of the Tanlu fault zone

The Tanlu Fault Zone is one of the largest fault zones in the eastern part of Eurasia. It originated from a collision between the NCC and the South China Plate during the Triassic and generally exhibits left-lateral strike-slip movement (Gilder et al., 1999; Hacker et al., 2006; Lei et al., 2020; Ma et al., 2020; Tian et al., 2020; Yin and Nie, 1993; Zhao et al., 2016; Zhu et al., 2017). The Tanlu Fault extends in a north-northeast direction and divides into two faults, the YYF and DMF, near Shenyang (Gu et al., 2016; Gu et al., 2017; Huang et al., 2015; Zhu et al., 2005). Our image results show that the YYF is a large, deep fault that cuts through the Moho (a crustal-scale fault) with a vertical offset of about 3 km. The YYF's position on the surface and impact on the Moho within the profile suggest that it dips to the northwest and experiences a degree of normal offset in addition to its generally recognized left-lateral strike-slip motion (dashed line in Fig. 5) (Gu et al., 2016; Gu et al., 2017; Min et al., 2013). The DMF does not obviously appear around the Moho and primarily exhibits steep, strike-slip motion in the study region.

5.2. The deep boundary between the NCC and the CAOB

Geological and geochemical studies interpret the NCC as Mesoproterozoic-Triassic sedimentary cover resting on an Archean-Paleoproterozoic metamorphic basement. The NCC was a stable, rigid block before the Mesozoic (Santosh et al., 2006; Santosh et al., 2007; Tang et al., 2015; Yang et al., 2016; Zhai and Santosh, 2011; Zhao et al., 2005). The accretionary zone in the north of the NCC consists primarily of early Paleozoic to Early Triassic metamorphic or volcanic-sedimentary rocks and Permian to Jurassic plutonic bodies (Pei et al., 2016; Wu et al., 2011; Yuan et al., 2016), which posses lower rigidity and strength than the underlying craton basement (Gu et al., 2018). This allows the discontinuity between the two parts to be imaged by the receiver function. We searched receiver function images for the contact area between the NCC and the accretionary zone. According to stacking receiver functions of each single station, a continuous positive seismic phase beneath the Songliao Basin penetrates from the surface down to the Moho (Fig. 4; Figs. 5-d1). The surface expression of this feature coincides with the CKF, or the inferred boundary between the NCC and CAOB (Xiao et al., 2003; Zhang et al., 2014). Results suggest that the d1 interface represents both the surface boundary between the NCC and CAOB, and its deep extension. The lower part (southeast part) of this interface exhibits high seismic wave velocity and a Vp/Vs ratio approaching average values for the entire profile. This represents the older, stable NCC component. By contrast, areas northwest of the interface exhibit low velocity and a relatively high Vp/Vs ratio. This reflects the accretionary complex formed during subduction of the Paleo-Asian Ocean beneath the NCC. It may have become a thrust nappe during final orogenic phases of the CAOB. As the CKF deepens into the CAOB, the Vp/Vs ratios show a gradual increase from south to north (Fig. 6-a). This may reflect the increase and thickening of the thrust nappe having the higher Vp/Vs ratio. It could also reflect the decrease of craton component having lower Vp/Vs ratio. Other areas of the profile indicate a NCC Vp/Vs ratio closer to the average value. The patterns in Vp/Vs confirm the crustal-scale thrust nappe system formed during the subduction-collision of the Paleo-Asian Ocean and NCC.

Theoretically, the accretion/nappe between the NCC and CAOB should be a belt-like region extending from east to west. We therefore considered additional geophysical profiles across surrounding belt-shaped geological areas (Roughly along the CKF) and compared them with our profile to better resolve the contact characteristics between the CAOB and NCC (Fig. 10). Due to the different distribution directions of the profiles, we transposed all profiles to a true north–south direction, that is roughly perpendicular to the CKF (Fig. 10-b). The deep reflection profile in the western part of the accretion belt indicates that a thrust nappe structure formed during the collision (Fig. 10-L1) (Zhang et al., 2014). The receiver function profile of the eastern part of the Yanshan Mountains along the northern margin of the NCC also displays a positive seismic phase corresponding to the inclined interface (Fig. 10-L2) (Zheng et al., 2007). The magnetic sounding profile on the west side of the Liaoyuan block shows the thrust nappe structure in the upper crust (Fig. 10-L3) (Xu et al., 2000). The three profiles show features consistent with those appearing in our profile. Together, the four profiles outline the deep interface for the entire accretion belt in an east–west direction. Additional geochemical evidence suggest ancient metamorphic rocks beneath the Songliao Basin similar to the NCC basement (Liu et al., 2019; Wang et al., 2006). Combining our results and previous studies above indicates that the northward boundary between the NCC and CAOB consists of a southward thrust nappe structure, along the CKF, which joins the two from the surface to deep. The deeper part of this boundary lies further to the north, possibly near the Xar Moron River suture zone. This means that the boundary between the NCC and CAOB gently dips to the north and represents a thrust feature.

6. Conclusions

(1) The Moho in the study area rests at a depth of about 32 km and exhibits a relatively flat orientation. Deep faults, some of which extend from the surface, cause local disruptions in the Moho. The

study area gave an average Vp/Vs ratio of around 1.75 with some location variations likely reflecting material composition changes around the block boundary and fault zone.

(2) The CKF in the study area represents the tectonic boundary between the NCC and CAOB on the surface. It appears as a north-dipping thrust nappe structure and may connect with the Xiramurun suture at depth. The upper part of the discontinuity (deep extension of CKF) is the thrust nappe structure of the CAOB, and the lower part is the NCC.

(3) The Tanlu Fault contains two branches, the YYF and the DMF. The former branch is an extensive, deep fault that cuts through the Moho to cause 2–3 km of displacement. The YYF dips to the northwest and shows normal offset likely caused by far field effects of Pacific Plate subduction. By contrast, the DMF branch shows no obvious displacement in the images interpreted here but may still experience sinistral strike-slip movement.

CRediT authorship contribution statement

Weiyu Dong: Conceptualization, Data curation, Formal analysis, Methodology, Software, Writing – original draft, Writing – review & editing. **Tao Xu:** Funding acquisition, Project administration, Investigation, Supervision, Writing – review & editing. **Yinshuang Ai:** Data curation, Project administration, Supervision. **Enbo Fan:** Formal analysis, Data curation. **Long Li:** Formal analysis, Data curation. **Jue Hou:** Data curation, Writing – review & editing.

Declaration of Competing Interest

The authors declare that they have no known competing financial interests or personal relationships that could have appeared to influence the work reported in this paper.

Data availability

The authors do not have permission to share data.

Acknowledgements

We appreciate the assistance of the IGGCAS Seismic Array Laboratory and the members of the NCISP10 field team who collected data for this study including Drs. Guangli Zhang, Haodong Zhang, Fanchang Meng, Minfu Huang and Fan Zheng. We are grateful to Profs. Tianyu Zheng, Laicheng Miao, Ling Chen, Wei Lin and Jinhui Yang, Drs. Zhenbo Wu, Youshan Liu and Xu Wang for the helpful discussions on the interpretation of our results. We gratefully acknowledge financial support for this research from the National Natural Science Foundation of China (42130807, 41804058, 41804060) and the National Key Research and Development Program of China (2016YFC0600101).

References

Bao, F., Li, Z., Yuen, D.A., Zhao, J., Ren, J., Tian, B., Meng, Q., 2018. Shallow structure of the Tangshan fault zone unveiled by dense seismic array and horizontal-to-vertical spectral ratio method. Phys. Earth Planet. Inter. 281, 46–54.

Chen, L., Tao, W., Zhao, L., Zheng, T., 2008. Distinct lateral variation of lithospheric thickness in the Northeastern North China Craton. Earth Planet. Sci. Lett. 267, 56–68.

Gilder, S.A., Leloup, P.H., Courtillot, V., Chen, Y., Coe, R.S., Zhao, X., Xiao, W., Halim, N., Cogné, J.-P., Zhu, R., 1999. Tectonic evolution of the Tancheng-Lujiang (Tan-Lu) fault via Middle Triassic to Early Cenozoic paleomagnetic data. J. Geophys. Res. B 104 (B7), 15365–15390.

Gu, C., Zhu, G., Zhai, M., Lin, S., Song, L., Liu, B., 2016. Features and origin time of Mesozoic strike-slip structures in the Yilan-Yitong Fault Zone. Sci. China 59 (12), 2389–2410.

Gu, C., Zhu, G., Zhang, S., Liu, C., Li, Y., Lin, S., Wang, W., 2017. Cenozoic evolution of the Yilan-Yitong Graben in NE China: An example of graben formation controlled by pre-existing structures. J. Asian Earth Sci. 146, 168–184.

Gu, C., Zhu, G., Li, Y., Su, N., Xiao, S., Zhang, S., Liu, C., 2018. Timing of deformation and location of the eastern Liaoyuan Terrane, NE China: Constraints on the final closure time of the Paleo-Asian Ocean. Gondwana Res. 60, 194–212.

Hacker, B.R., Wallis, S.R., Ratschbacher, L., Grove, M., Gehrels, G., 2006. High-temperature geochronology constraints on the tectonic history and architecture of the ultrahigh-pressure Dabie-Sulu Orogen. Tectonics 25 (5).

He, Y., Chen, Q., Chen, L., Wang, X., Guo, G., Li, T., Zhang, K., Li, J., Chen, Y., 2021. Distinct Lithospheric Structure in the Xing'an-Mongolian Orogenic Belt. Geophys. Res. Lett. 49.

Huang, S., Dong, S., Zhang, Y., Zhang, F., Huang, D., Wei, S., Li, Z., Miao, L., Zhu, M., 2015. The deformation and tectonic evolution of the Huahui Basin, northeast China, during the Cretaceous-Early Cenozoic. J. Asian Earth Sci. 114, 717–731.

Kröner, A., Kovach, V., Belousova, E., Hegner, E., Armstrong, R., Dolgopolova, A., Seltmann, R., Alexeiev, D.V., Hoffmann, J.E., Wong, J., Sun, M., Cai, K., Wang, T., Tong, Y., Wilde, S.A., Degtyarev, K.E., Rytsk, E., 2014. Reassessment of continental growth during the accretionary history of the Central Asian Orogenic Belt. Gondwana Res. 25 (1), 103–125.

Lei, J., Zhao, D., Xu, X., Du, M., Mi, Q., Lu, M., 2020. P-wave upper-mantle tomography of the Tanlu fault zone in eastern China. Phys. Earth Planet. Inter. 299, 106402.

Lei, J., Zhao, D., 2005. P-wave tomography and origin of the Changbai intraplate volcano in Northeast Asia. Tectonophysics 397 (3-4), 281–295.

Lei, J., Zhao, D., 2006. Global P-wave tomography: On the effect of various mantle and core phases. Phys. Earth Planet. Inter. 154 (1), 44–69.

Ligorrfa, J.P., Ammon, C.J., 1999. Iterative Deconvolution and Receiver-Function Estimation. Bull. Seismol. Soc. Am. 5, 1395–1400.

Liu, Y., Li, W., Feng, Z., Wen, Q., Neubauer, F., Liang, C., 2017. A review of the Paleozoic tectonics in the eastern part of Central Asian Orogenic Belt. Gondwana Res. 43, 123–148.

Liu, C., Zhu, G., Xie, C., Zhang, S., Li, Y., Su, N., Xiao, S., 2019. Location and sinistral displacement of the eastern Liaoyuan Accretionary Belt along the Tan-Lu Fault Zone. NE China. J. Asian Earth Sci. 172, 409–422.

Ma, C., Lei, J., Xu, X., 2020. Three-dimensional shear-wave velocity structure under the Weifang segment of the Tanlu fault zone in eastern China inferred from ambient noise tomography with a short-period dense seismic array. Phys. Earth Planet. Inter. 309, 106590.

Meng, F., Ai, Y., Xu, T., Chen, L., Wang, X., Li, L., 2021. Lithospheric structure beneath the boundary region of North China Craton and Xing Meng Orogenic Belt from S-receiver function analysis. Tectonophysics 818, 229067.

Meng, Q.-R., Zhang, G.-W., 2000. Geologic framework and tectonic evolution of the Qinling orogen, central China. Tectonophysics 323 (3-4), 183–196.

Min, W., Liu, Y., Jiao, D., Shen, J., Pan, X., 2013. Evidence for Holocene activity of the Yilan-Yitong fault, northeastern section of the Tan-Lu fault zone in Northeast China. J. Asian Earth Sci. 67–68, 207–216.

Pei, F., Zhang, Y., Wang, Z., Cao, H., Xu, W., Wang, Z., Wang, F., Yang, C., 2016. Early-Middle Paleozoic subduction-collision history of the south-eastern Central Asian Orogenic Belt: Evidence from igneous and metasedimentary rocks of central Jilin Province, NE China. Lithos 261, 164–180.

Santosh, M., Sajeev, K., Li, J.H., 2006. Extreme crustal metamorphism during Columbia supercontinent assembly: Evidence from North China Craton. Gondwana Res. 10 (3-4), 256–266.

Santosh, M., Tsunogae, T., Li, J.H., Liu, S.J., 2007. Discovery of sapphirine-bearing Mg-Al granulites in the North China Craton: Implications for Paleoproterozoic ultrahigh temperature metamorphism. Gondwana Res. 11 (3), 263–285.

Santosh, M., Sajeev, K., Li, J.H., Liu, S.J., Itaya, T., 2009. Counterclockwise exhumation of a hot orogen: The Paleoproterozoic ultrahigh-temperature granulites in the North China Craton. Lithos 110 (1-4), 140–152.

Tang, L., Santosh, M., Teng, X., 2015. Paleoproterozoic (ca. 2.1-2.0Ga) arc magmatism in the Fuping Complex: Implications for the tectonic evolution of the Trans-North China Orogen. Precambrian Res. 268, 16–32.

Tang, L., Santosh, M., Tsunogae, T., Maruoka, T., 2016. Paleoproterozoic meta-carbonates from the central segment of the Trans-North China Orogen: Zircon U-Pb geochronology, geochemistry, and carbon and oxygen isotopes. Precambrian Res. 284, 14–29.

Tao, K., Liu, T., Ning, J., Niu, F., 2014. Estimating sedimentary and crustal structure using wavefield continuation: theory, techniques and applications. Geophys. J. Int. 197, 443–457.

Tian, F., Lei, J., Xu, X., 2020. Teleseismic P-wave crustal tomography of the Weifang segment on the Tanlu fault zone: A case study based on short-period dense seismic array experiment. Phys. Earth Planet. Inter. 306, 106521.

Wang, Y., Zhang, F., Zhang, D., Miao, L., Li, T., Xie, H., Meng, Q., Liu, D., 2006. Zircon SHRIMP U-Pb dating of metadiorites in the southern Songliao Basin and its geological significance(in Chinese). Sci. China 51, 1811–1816.

Wilde, S.A., 2015. Final amalgamation of the Central Asian Orogenic Belt in NE China: Paleo-Asian Ocean closure versus Paleo-Pacific plate subduction-A review of the evidence. Tectonophysics 662, 345–362.

Windley, B.F., Alexeiev, D., Xiao, W., Kröner, A., Badarch, G., 2007. Tectonic models for accretion of the Central Asian Orogenic Belt. JGS 164 (1), 31–47.

Wu, F., Lin, J., Wilde, S., Zhang, X., Yang, J., 2005. Nature and significance of the Early Cretaceous giant igneous event in eastern China. Earth Planet. Sci. Lett. 233 (1-2), 103–119.

Wu, C., Xu, T., Ai, Y., Dong, W., Li, L., 2020. XKS splitting-based upper-mantle deformation in the Jiaodong Peninsula records the boundary between the North China Craton and South China Block. Geophys. J. Int. 222, 956–964.

Wu, C., Xu, T., Ai, Y., Dong, W., Li, L., Hou, J., 2021. Crustal azimuthal anisotropy in the Jiaodong Peninsula: Evidence for the suture between the North China Craton and South China Block. Phys. Earth Planet. Inter. 314.

Wu, F.-Y., Zhao, G.-C., Sun, D.-Y., Wilde, S.A., Yang, J.-H., 2007. The Hulan Group: Its role in the evolution of the Central Asian Orogenic Belt of NE China. J. Asian Earth Sci. 30 (3-4), 542–556.
Wu, F.-Y., Sun, D.-Y., Ge, W.-C., Zhang, Y.-B., Grant, M.L., Wilde, S.A., Jahn, B.-M., 2011. Geochronology of the Phanerozoic granitoids in northeastern China. J. Asian Earth Sci. 41 (1), 1–30.
Xiao, W., Windley, B.F., Hao, J., Zhai, M., 2003. Accretion leading to collision and the Permian Solonker suture. Tectonics 22 (6).
Xiao, W., Windley, B.F., Sun, S., Li, J., Huang, B., Han, C., Yuan, C., Sun, M., Chen, H., 2015. A Tale of Amalgamation of three Permo-Triassic Collage systems in Central Asia: Oroclines, Sutures, and Terminal Accretion. Annu. Rev. Earth Planet. Sci. 43 (1), 477–507.
Xu, M., Middleton, M.F., Xue, L.F., Wang, D.P., 2000. Structure of the Lithosphere and Mesozoic Sedimentary Basins in Western Liaoning, Northern Liaoning, and Songliao, Northeast China. Int. Geol. Rev. 42 (3), 269–278.
Yang, Y., Lei, J., Ai, Y., Zhang, G., Sun, C., Fan, E., Li, L., Mi, Q., Lu, M., He, J., Wang, J., Du, M., Zhang, B., Tian, F., Ma, C., Liu, Z., 2019. Crustal structure beneath Northeast China from ambient noise tomography. Phys. Earth Planet. Inter. 293, 106257.
Yang, Q., Santosh, M., Collins, A.S., Teng, X., 2016. Microblock amalgamation in the North China Craton: Evidence from Neoarchaean magmatic suite in the western margin of the Jiaoliao Block. Gondwana Res. 31, 96–123.
Yin, A.n., Nie, S., 1993. An indentation model for the north and south china collision and the development of the Tan-lu and Honam fault systems, eastern Asia. Tectonics 12 (4), 801–813.
Yu, Y., Song, J., Liu, K.H., Gao, S.S., 2015. Determining crustal structure beneath seismic stations overlying a low-velocity sedimentary layer using receiver functions. J. Geophys. Res. 120 (5), 3208–3218.
Yuan, L., Zhang, X., Xue, F., Lu, Y., Zong, K., 2016. Late Permian high-Mg andesite and basalt association from northern Liaoning, North China: Insights into the final closure of the Paleo-Asian ocean and the orogen-craton boundary. Lithos 258–259, 58–76.
Zhai, M., Santosh, M., 2011. The early Precambrian odyssey of the North China Craton: A synoptic overview. Gondwana Res. 20, 6–25.
Zhai, M., Santosh, M., 2013. Metallogeny of the North China Craton: Link with secular changes in the evolving Earth. Gondwana Res. 24, 275–297.
Zhang, S., Gao, R., Li, H., Hou, H., Wu, H., Li, Q., Yang, K., Li, C., Li, W., Zhang, J., Yang, T., G., R. K., Liu, M., 2014. Crustal structures revealed from a deep seismic reflection profile across the Solonker suture zone of the Central Asian Orogenic Belt, northern China: An integrated interpretation. Tectonophysics, 26-39.
Zhang, B., Zhu, G., Jiang, D., Li, C., Chen, Y., 2012. Evolution of the Yiwulushan metamorphic core complex from distributed to localized deformation and its tectonic implications. Tectonics 31.
Zhang, B., Lei, J., Yuan, X., Zhang, G., He, J., Xu, Q., 2020. Detailed Moho variations under Northeast China inferred from receiver function analyses and their tectonic implications. Phys. Earth Planet. Inter. 300, 106448.
Zhang, S., Zhao, Y., Song, B., Yang, Z., Hu, J., Wu, H., 2007. Carboniferous granitic plutons from the northern margin of the North China block: implications for a late Palaeozoic active continental margin. J. Geol. Soc. London 164, 451–463.
Zhang, R., Wu, Q., Sun, L., He, J., Gao, Z., 2014. Crustal and lithospheric structure of Northeast China from S-wave receiver functions. Earth Planet. Sci. Lett. 401, 196–205.
Zhang, S., Zhao, Y., Song, B., Hu, J., Liu, S., Yang, Y., Chen, F., Liu, X., Liu, J., 2009. Contrasting Late Carboniferous and Late Permian-Middle Triassic intrusive suites from the northern margin of the North China craton: Geochronology, petrogenesis, and tectonic implications. Geol. Soc. Am. Bull. 121, 181–200.
Zhao, G., Sun, M., Wilde, S.A., Sanzhong, L., 2005. Late Archean to Paleoproterozoic evolution of the North China Craton: key issues revisited. Precambrian Res. 136, 177–202.
Zhao, G., Zhai, M., 2013. Lithotectonic elements of Precambrian basement in the North China Craton: Review and tectonic implications. Gondwana Res. 23, 1207–1240.
Zhao, T., Zhu, G., Lin, S., Wang, H., 2016. Indentation-induced tearing of a subducting continent: Evidence from the Tan-Lu Fault Zone, East China. Earth-Sci. Rev. 152, 14–36.
Zheng, T., Chen, L., Zhao, L., Zhu, R., 2007. Crustal structure across the Yanshan belt at the northern margin of the North China Craton. Phys. Earth Planet. Inter. 161, 36–49.
Zhu, L., 2000a. Crustal structure across the San Andreas Fault, southern California from teleseismic converted waves. Earth Planet. Sci. Lett. 179, 183–190.
Zhu, L., 2000b. Moho depth variation in southern California. J. Geophys. Res. B 2, 2969–2980.
Zhu, G., Wang, Y., Liu, G., Niu, M., Xie, C., Li, C., 2005. 40Ar/39Ar dating of strike-slip motion on the Tan-Lu fault zone, East China. J. Struct. Geol. 27, 1379–1398.
Zhu, G., Jiang, D., Zhang, B., Chen, Y., 2012. Destruction of the eastern North China Craton in a backarc setting: Evidence from crustal deformation kinematics. Gondwana Res. 22, 86–103.
Zhu, G., Chen, Y., Jiang, D., Lin, S., 2015. Rapid change from compression to extension in the North China Craton during the Early Cretaceous: Evidence from the Yunmengshan metamorphic core complex. Tectonophysics 656, 91–110.
Zhu, G., Wang, Y., Wang, W., Zhang, S., Liu, C., Gu, C., Li, Y., 2017. An accreted micro-continent in the north of the Dabie Orogen, East China: Evidence from detrital zircon dating. Tectonophysics 698, 47–64.